Oxidized sulfur species in slab fluids as a source of enriched sulfur isotope signatures in arcs

Patrick Beaudry[1] and Dimitri A. Sverjensky[1]

[1]Department of Earth and Planetary Sciences, Johns Hopkins University, Baltimore, MD, USA

Corresponding author: Patrick Beaudry (pbeaudr1@jhu.edu)

Key Points:

- We analyzed high pressure experimental solubilities of anhydrite to calibrate the properties of aqueous S species in the Deep Earth Water model.
- We provide a template for the solubility and speciation of S and other rock-forming elements in a wide hypothetical range of subduction fluids.
- It can be expected that fluids are ^{34}S-rich relative to slabs due to high concentrations of sulfate complexes in equilibrium with pyrite.

Abstract

Recycling of oxidized sulfur from subducting slabs to the mantle wedge provides simultaneous explanations for the elevated oxygen fugacity (fO_2) in subduction zones, their high hydrothermal and magmatic sulfur outputs, and the enriched sulfur isotopic signatures (i.e. $\delta^{34}S > 0‰$) of these outputs. However, a quantitative understanding of the abundance and speciation of sulfur in slab fluids consistent with high pressure experiments is lacking. Here we analyze published experimental data for anhydrite solubility in H_2O–NaCl solutions to calibrate a high-pressure aqueous speciation model of sulfur within the framework of the Deep Earth Water model. We characterize new species, required to account for the high experimental anhydrite solubilities. We then use this framework to predict the speciation and solubility of sulfur in chemically complex fluids in equilibrium with subducting mafic and ultramafic lithologies, from 2 to 3 GPa and 400 to 800°C at log fO_2 from FMQ-2 to FMQ+4. We show that sulfate complexes of calcium and sodium markedly enhance the stability of sulfate in moderately oxidized fluids in equilibrium with pyrite at fO_2 conditions of FMQ+1 to +2, causing large sulfur isotope fractionations up to 10‰ in the fluid relative to the slab. Such fluids could impart oxidized, sulfur-rich and high $\delta^{34}S$ signatures to the mantle wedge that are ultimately transferred to arc magmas, without the need to invoke ^{34}S-rich subducted lithologies.

Plain Language Summary

Subducting oceanic plates (or "slabs") release aqueous fluids when subjected to high pressures and temperatures, driving the magmatism that produces volcanic arcs along subduction zones. These fluids carry high concentrations of solutes, and thus play an important role in the geologic cycling of elements. Of particular interest are the abundance and redox state of sulfur, since the transfer of sulfur-rich fluids could explain the high oxidation state of arc magmas, the observation that they are often sulfur-rich, as well as their heavy sulfur isotope signatures (i.e. enriched in ^{34}S relative to bulk Earth). However, there is conflicting evidence about sulfur's oxidation potential and the origin and significance of its isotopic enrichment. To address this problem, we need to understand which sulfur-bearing chemical species are important at high pressures and temperatures relevant to subduction zone conditions. To do this, we analyzed high-pressure experimental data, and found that they could be explained by the presence of aqueous species such as $CaHSO_4^+$ and $Na_2SO_4^0$, previously uncharacterized at high temperatures and pressures, in which sulfur is in its oxidized form. We further predict that these species would be important in natural subduction zone fluids and would carry enrichments in ^{34}S, which can explain the enriched sulfur isotope signatures typically observed in arc volcanic rocks and gases.

1. Introduction

Aqueous fluids released by subducting slabs enable mass and chemical exchange across subduction zones. Fluid-driven metasomatism of the mantle wedge is recorded in exhumed metamorphic rocks (Bebout & Penniston-Dorland, 2016; Scambelluri et al., 2014; Walters et al., 2019), and element recycling is deduced from the unique trace element geochemistry of arc magmas (Class et al., 2000; Grove et al., 2002; Kessel et al., 2005). However, our understanding of the chemistry of subduction zone fluids is still limited because these fluids are not directly accessible. Instead, knowledge of their properties relies on experimental solubilities of minerals and rocks incorporated into thermodynamic modelling. Such work predicts significantly increased solute concentrations at the high pressures and temperatures relevant to subduction zone conditions (Huang & Sverjensky, 2019; Manning, 2004). In situ spectroscopic studies of experimentally-produced

fluids also provide important information about fluid speciation (Colin et al., 2020; Schmidt & Seward, 2017).

There are several lines of evidence indicating that the mantle wedge above subduction zones becomes oxidized (Brounce et al., 2021; Carmichael, 1991; Evans, 2012; Parkinson & Arculus, 1999), but the exact mechanisms by which this occurs remain elusive. It has been suggested that oxidized sulfur species are prevalent in slab fluids, hence they are among the preferred candidates for oxidizing the mantle wedge (Ague et al., 2022; Bénard et al., 2018; Debret & Sverjensky, 2017; Padrón-Navarta et al., 2023; Tomkins & Evans, 2015; Walters et al., 2020). The cycling of oxidized sulfur in subduction zones may also be particularly important for interpreting sulfur-rich volcanic eruptions as well as the emplacement of porphyry Cu-Au deposits along volcanic arcs (Richards, 2011; P.J. Wallace, 2001; Wilkinson, 2013). Furthermore, heavy $\delta^{34}S$ values typically occur in arc-related lavas and volcanic gases, which has been interpreted to reflect the transfer of isotopically enriched sulfate from the slab (Alt et al., 1993; Bénard et al., 2018; de Moor et al., 2022; Muth & Wallace, 2021; Taracsák et al., 2023). However, conflicting evidence points to other possible scenarios, such as isotopic fractionation during partial melting or differentiation of oxidized magmas (Li et al., 2020; Rezeau et al., 2023).

Thermodynamic predictions suggest that oxidized sulfur species dominate the flux of slab-derived sulfur from altered oceanic crust, supporting the idea that it could oxidize the mantle wedge (Walters et al., 2020). However, robust constraints on the high-pressure nature of aqueous sulfate species, including the effect of NaCl, are lacking from current thermodynamic databases, which limits our understanding of sulfur speciation in slab fluids. Here we integrate high-pressure experimental solubilities of anhydrite (Newton & Manning, 2005) into the thermodynamic framework of the extended Deep Earth Water (DEW) model (Huang & Sverjensky, 2019; Sverjensky et al., 2014) to establish new high-pressure sulfate and chloride speciation. As a consequence, we can predict the speciation and concentration of sulfur in slab-derived fluids over a wide range of oxidation states in chloride-bearing fluids. This improves our ability to evaluate the potential role of sulfur as an oxidizing agent, and to interpret the sulfur isotope compositions of arc volcanic products.

2. Methods

2.1. Regression of experimental solubility data

Although anhydrite is not expected in metamorphic mineral assemblages, its solubility represents an upper limit for sulfate species in subduction zones. Knowledge of anhydrite solubility at elevated temperatures and pressures is therefore important. Furthermore, the aqueous sulfur species in equilibrium with anhydrite may also be important in fluids in equilibrium with other sulfur-bearing minerals (e.g. pyrite, see below). Although the solubility in NaCl solutions has been measured at elevated temperatures and pressures (Newton & Manning, 2005), these experimental data have only been applied to subduction zones as stoichiometric solubilities, i.e. assuming that the total dissolved calcium molality ($m_{t,Ca}$) equals the sulfate molality ($m_{t,S}$), e.g. Tomkins and Evans (2015). However, in subducting mineral assemblages, the molality of calcium is constrained by equilibria between the fluid and silicate mineral assemblages. Under these circumstances, the values of $m_{t,Ca}$ and $m_{t,S}$ in a fluid also in equilibrium with anhydrite should be different from one another. It is therefore crucial that the experimental solubilities of anhydrite be analysed with an aqueous speciation and solubility model. The results can then be incorporated into comprehensive aqueous speciation, solubility and mass transfer models of natural assemblages where $m_{t,Ca}$ will not in general be equal to $m_{t,S}$. It will be shown below that $m_{t,Ca}$ values in model subduction zone

fluids can be less than $m_{t,S}$ values, resulting in solubilities of sulfate much higher than stoichiometric values of anhydrite solubility.

Several studies have investigated the solubility of anhydrite in H_2O–NaCl solutions (e.g. see compilation by Creaser et al., 2022), but only one experimental study (Newton & Manning, 2005) reports anhydrite solubility data at high pressures >0.5 GPa applicable to subduction zone fluids. It is also important to realize that the solubility behavior changes drastically above 0.1 GPa (Blount & Dickson, 1969; Newton & Manning, 2005). Hence it is our priority to model high pressure solubility.

2.1.1. Modelling of anhydrite solubility in water

Here we regressed anhydrite solubility data using the aqueous speciation and solubility software EQ3 (Wolery, 1992) modified for elevated pressures and temperatures as described previously. We initially used equilibrium constants of aqueous ions and metal complexes from the Deep Earth Water (DEW) model (Huang & Sverjensky, 2019; Sverjensky et al., 2014), which has provided a new equation of state for the dielectric constant of water, enabling calculations up to 6 GPa and 1000°C. Input parameters were pressure, temperature, fO_2 and pH. We varied the pH at given fO_2 conditions to obtain equimolar concentrations of Ca and S in the fluid, as would occur during the experimental stoichiometric dissolution of anhydrite ($CaSO_4$). Sulfur-bearing species included in the DEW2019 database (Huang & Sverjensky, 2019) were H_2S, HS^-, HSO_4^-, SO_4^{2-}, $CaSO_4^0$, $MgSO_4^0$, $NaSO_4^-$ and KSO_4^-, for which equation of state parameters were previously established. We excluded aqueous sulfite species ($SO_2(aq)$, HSO_3^- and SO_3^{2-}) from our calculations, because they, and possible complexes involving them, have not been characterized at high pressures and temperatures. Nevertheless, we calculated their effect in the regression of anhydrite solubility data, using their equation of state coefficients from the DEW2019 model (Fig. S1).

We first analysed anhydrite solubility data in water at 1 GPa (Newton & Manning, 2005). It can be seen in **Fig. 1a** that the computed anhydrite solubilities in the simple H_2O–$CaSO_4$ system strongly underestimate much of the experimental data when only considering the sulfur species included in DEW2019 model (Huang & Sverjensky, 2019). The mismatch demonstrates that important sulfur species were missing from this model. Importantly, Fig 1 shows a pronounced mismatch at oxidizing conditions (e.g. FMQ+4), while the estimated solubility at the NNO buffer (FMQ+0.25) is close to that calculated with the original DEW model. This suggests that reduced S-species are well characterized, but that one or more oxidized species are missing. The inclusion of sulfite species does not satisfy this mismatch (Fig. S1). In our model fluids at oxidizing conditions, bisulfate was far more abundant than sulfate at elevated temperatures, suggesting the need for a Ca-bisulfate complex. We therefore included the $CaHSO_4^+$ complex ion, according to the reaction

$$CaHSO_4^+ \rightleftharpoons Ca^{2+} + HSO_4^- \quad \text{(Eq. 1)}$$

Little is known about this complex ion, apart from one estimate of its equilibrium constant at 25°C and 1 bar from the WATEQ4F software based on (Mattigod & Sposito, 1977). However, by using the experiments of Newton and Manning (2005) in the H_2O–$CaSO_4$ system, we retrieved values of its equilibrium constant at several temperatures and pressures (Table 1). This requires estimating fO_2 for unbuffered experiments, which can be done given that we have low and high fO_2 constraints at 800°C, and that anhydrite solubility in unbuffered experiments is intermediate. In Fig. 1a it can be seen that our model curve for the HM buffer is fixed on the experimental data at 800°C. This was achieved by adjusting values for the equilibrium constant for Eq. 1 at 800°C (Table 1). This

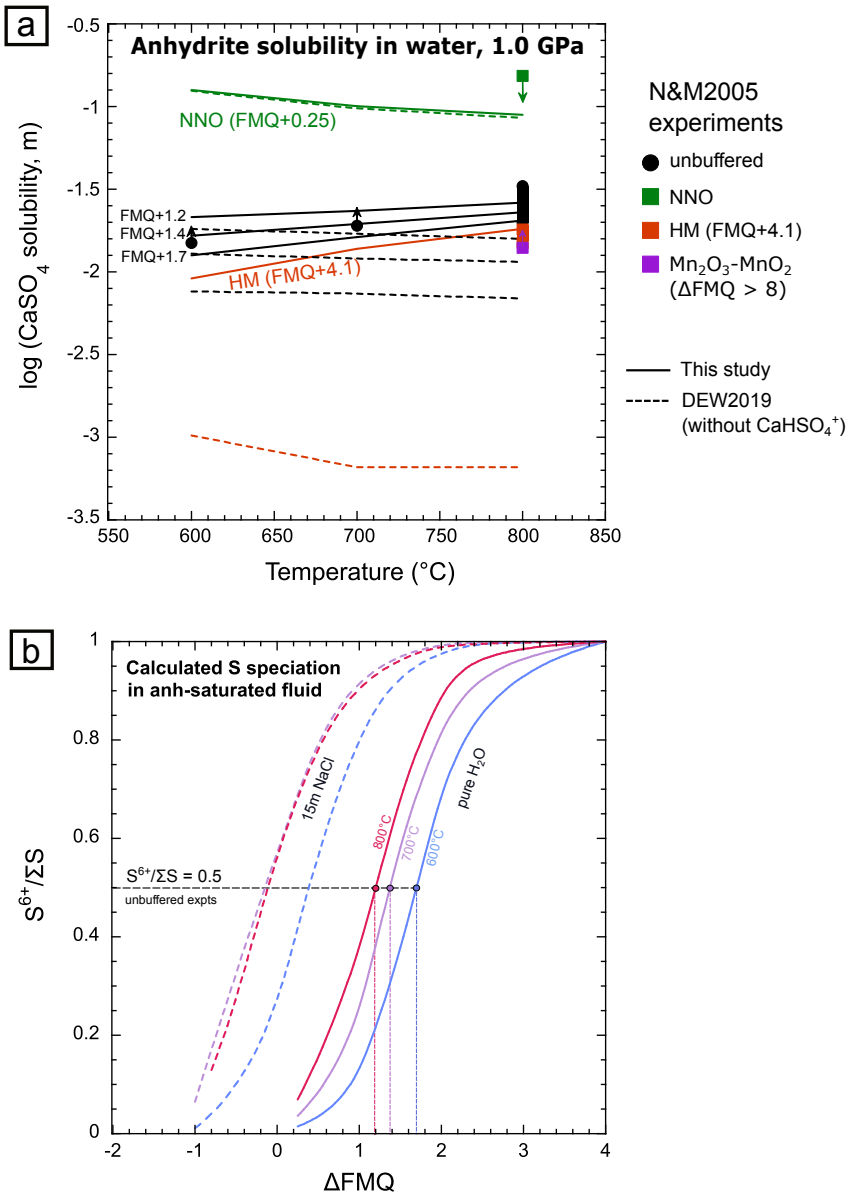

Figure 1: (a) Regression of experimental anhydrite ($CaSO_4$) solubility data in pure water at 1.0 GPa from Newton and Manning (2005), showing solubility vs temperature at different log fO_2 values. Symbols represent experimental data and lines represent model calculations. Arrows represent minimum or maximum estimates of experimental solubilities. The solid curves represent calibration of a $CaHSO_4^+$ complex and are labelled with fO_2 expressed in log units relative to the buffers FMQ: Fayalite–magnetite–quartz; NNO: Nickel–nickel oxide; and HM: Hematite–magnetite. Dashed curves show the calculated solubilities using the DEW2019 model, which did not include $CaHSO_4^+$. In **(b)** we show the adopted fO_2 in our calculations at different temperatures in unbufferred experiments, assuming that 50% of the sulfur is in its oxidized state ($S^{6+}/\Sigma S = 0.5$); data shown in (a) suggest that both sulfide (S^{2-}) and sulfate (S^{6+}) are present.

enabled prediction of the NNO curve which is consistent with the upper limit of the experimental solubility at 800°C at NNO. The predicted curves for the unbuffered experiments at intermediate

oxidation states are also shown in Fig. 1a. Anhydrite solubilities in unbuffered experiments are intermediate to those at NNO and HM, hence those fluids must contain both reduced and oxidized species. Because the transition from reduced to oxidized sulfur species occurs over a relatively narrow range of $\log f_{O_2}$ values (Fig. 1b), we assumed equal proportions of reduced and oxidized sulfur (i.e. $S^{6+}/\Sigma S = 0.5$) to obtain a reasonable approximation of $\log f_{O_2}$ (Fig. 1b).

Good agreement can be seen in Fig. 1a for the model unbuffered curves and the experimental unbuffered data. The solubility decreases with increasing fO_2 due to a steep decrease in the concentrations of reduced species (H_2S and HS^-) and increasing anhydrite stability. Importantly, it can be seen in Fig. 1a that the solubilities in the unbuffered experiments in water at ~FMQ+1 to FMQ+2 are low, about 0.03 to 0.02 m. We keep the conventional notation in log fO_2 units relative to the fayalite-magnetite-quartz (FMQ) buffer, but it is important to realize that no silicate minerals were present in these experiments.

We also note that the new $CaHSO_4^+$ species does not change significantly the predicted anhydrite solubility along the vapor saturation curve, such that experimental data at these conditions (Blount & Dickson, 1969) can still be reproduced by our model.

Table 1: Dissociation constants (log K values) of aqueous species determined from experimental anhydrite solubility data in pure water ($CaHSO_4^+$) and H_2O–NaCl solutions ($Na_2SO_4{}^0_{aq}$ and $CaCl_2{}^0_{aq}$).

T (°C)	$\log f_{O_2}$ min[a]	$\log f_{O_2}$ max[a]	$CaHSO_4^+$		$Na_2SO_4{}^0_{aq}$		$CaCl_2{}^0_{aq}$	
			$\log K_{min}$	$\log K_{max}$	$\log K_{min}$	$\log K_{max}$	$\log K_{min}$	$\log K_{max}$
600	FMQ+1.5	FMQ+2	-5.9	-5.4	-3.9	-2.9	-3.9	-3.5
700	FMQ+1.2	FMQ+1.7	-6.4	-5.9	-5.8	-4.1	-5.0	-4.6
800	FMQ	FMQ+1.5	-7.0	-6.6	-7.0	-5.0	-6.6	-5.5

[a] Values of $\log f_{O_2}$ at the FMQ buffer at 1.0 GPa are -18.8 (600°C), -15.9 (700°C) and -13.6 (800°C).

2.1.2. Modelling anhydrite solubility in NaCl solutions

Our second step in analyzing anhydrite solubility involved NaCl solutions. At high salinities, it can be expected that aqueous activity coefficents and additional aqueous complexes could be important contributers to the solubility models. Our assumptions for aqueous activity coefficients are summarized here first.

Activity coefficients of the species added to the DEW model in this work were treated in the same manner as that described in detail by Sverjensky (2019). For ionic species (e.g. $CaHSO_4^+$, S_3^-), activity coefficients were represented by

$$\log \bar{\gamma}_{P,T} = -\frac{A_\gamma Z_j^2 \bar{I}^{0.5}}{1+a_k B_\gamma \bar{I}^{0.5}} + b_{\gamma,k}\bar{I} + \Gamma_\gamma \qquad \text{(Eq. 2)}$$

The first term on the right-hand side is the Debye-Hückel term, where A_γ and B_γ are functions of temperature, density and dielectric constant of water, and $\bar{I}$ is the ionic strength of the solution. The second term is related to solvation and short-range interactions and referred to as the extended term. In the absence of reliable independent estimates, $b_{\gamma,k}$ was assumed to be 0. The last term is a conversion factor from the mole fraction to the molality concentration scale:

$$\Gamma_\gamma = -\log (1+0.0180153m^*) \quad \text{(Eq. 3)}$$

where m^* is the sum of the molalities of all aqueous species in the solution.

For a neutral species n (e.g. $Na_2SO_4^0$, $CaCl_2^0$), the activity coefficient is expressed as:

$$\log \bar{\gamma}_{n;P,T} = b_{n,k}\bar{I} + \Gamma_\gamma \quad \text{(Eq. 4)}$$

which is similar to the ionic case (Eq. 2) without the Debye-Hückel term. Here again, we assumed the $b_{n,k}$ term to be 0. However, we retained the second term (Γ_γ) because it becomes important in concentrated solutions, such as at the high NaCl molalities attained in the experiments of Newton & Manning (2005). The effect of Γ_γ can be seen in Fig. 2a, where the thicker curves take into account the increasing effect of activity coefficients on the activities of the neutral complexes $Na_2SO_4^0$ and $CaCl_2^0$, which produces a slight curvature, as expected from the experimental data. The families of thin curves shown for each temperature have a more linear profile and poorer fit to the experimental data. Overall, uncertainties in assigning activity coefficients are probably minor compared with the uncertainties in establishing and quantifying the equilibrium constants of the principal complexes responsible for the measured solubilities of anydrite in saline fluids (Fig. 3).

The strong positive effect of NaCl on the solubility of anhydrite observed by Newton & Manning (2005) led them to suggest that the dissolution of anhydrite in NaCl-bearing solutions was governed by the reaction:

$$CaSO_4 + 2NaCl \rightleftharpoons CaCl_2 + Na_2SO_4 \quad \text{(Eq. 5)}$$

Our $CaHSO_4^+$ species produces only a small increase in the calculated anhydrite solubility with increasing NaCl content, way below the experimental solubility data (Fig. 2a). Accordingly, we regressed the experimental solubilities to obtain revised equilibrium constants for the $CaCl_2^0$ complex different from those previously predicted (Huang & Sverjensky, 2019; Sverjensky et al., 1997) simultaneously with those of the species $Na_2SO_4^0$ not previously used in the DEW model (Table 1). To remain consistent with our regression of experimental solubility in pure water (Fig. 1a), we adopted the same log fO$_2$ values as those used in unbuffered runs (Fig. 1b), because the experiments using NaCl solutions were also unbuffered. It should be noted that the positions of the curves in Fig. 2a are insensitive to the values of log fO$_2$ used because the strong $Na_2SO_4^0$ complex stabilizes sulfate species relative to reduced sulfur species in $NaCl$-rich fluids (Fig. 1b). The bold solid curves in Fig. 2a represent our best fit to the experimental solubilities over a very wide range of $NaCl$ concentrations and temperatures ranging from 600–800°C at 10.0 kbar. Although the bold curves in Fig. 2a do not exactly reproduce the quadratic curvature of the experimental data, they nevertheless reproduce the expected increase and approximate slope of the data, which strongly supports our characterization of the $CaCl_2^0$ and $Na_2SO_4^0$ complexes. The curves are consistent with our final equilibrium constants retrieved for $Na_2SO_4^0$ and $CaCl_2^0$ (Table 1) and plotted versus temperature in Fig. 3c,d.

The solid cuves in Figs. 3a-d represent regression of the equilibrium constants from Table 1 and the literature using the revised Helgeson-Kirkham-Flowers (HKF) equations of state (Shock et al., 1989; Shock & Helgeson, 1988) including correlations between the standard partial molal properties of the complexes and their equation of state coefficients developed in Shock & Helgeson

(1988) and Sverjensky et al. (2014) and summarized in (Sverjensky, 2019). All the parameters are documented in Table 2. Our thermodynamic properties for the $Na_2SO_4^0$ complex are based on the

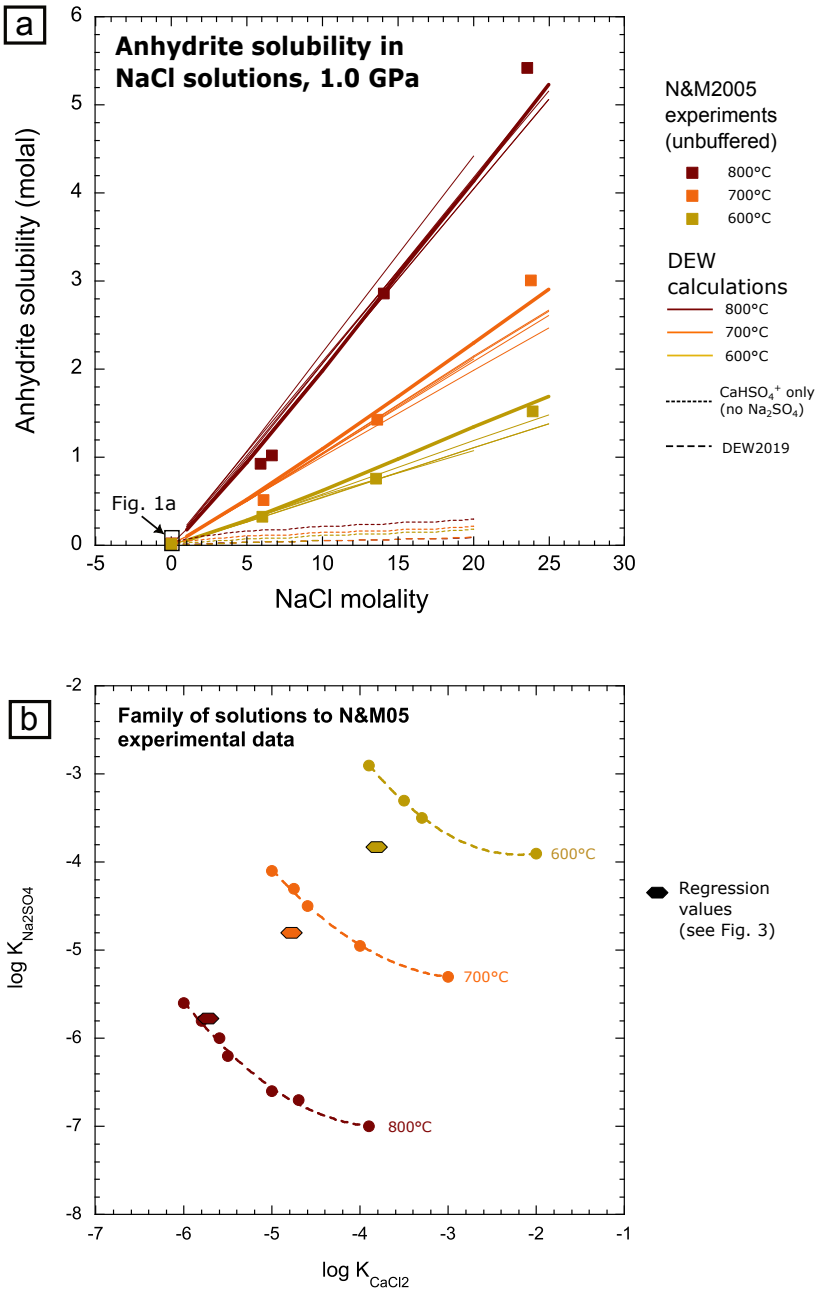

Figure 2: Use of the Newton and Manning (2005) experimental data to characterise the $Na_2SO_4^0$ and $CaCl_2^0$ complexes. The extreme solubilities of anhydrite at high NaCl molalities are only reproduced when considering the effect of the $Na_2SO_4^0$ aqueous complex, as shown by the solid curves in (a); dashed lines near 0 show the solubilities calculated with the DEW2019 models, while dotted lines reaching solubilities of ~0.1 to 0.3m shown the solubilities calculated when considering $CaHSO_4^+$ but not $Na_2SO_4^0$. Bold curves (one for each temperature) incorporate activity coefficients for neutral species. The families of curves shown for each temperature represent different combinations of log K's for $Na_2SO_4^0$ and $CaCl_2^0$, shown as individual dots in (b). Hexagonal symbols show the log K values used in the regressions in Fig. 3.

study of Hnedkovsky et al. (2005) (Fig. 3c) and the experimental data in Fig. 2a. We found that various combinations of log K's for the two species could be used to optimize the fit to Newton and Manning's experimental data as shown in Fig. 2b. To restrict this range, additional constraints were provided by predictive correlations for the standard partial molal entropies and heat capacities at 25°C and 1.0 bar from the HKF approach (Sverjensky et al., 1997; Sverjensky, 2019). In addition, standard partial molar volumes $\bar{V}^0$ of the complex species were estimated from the a_1 equation of state coefficients for the constituent ions. This is based on the prediction that the sum of intrinsic volume coefficients should satisfy $\sum \nu_i a_i = 0$. We integrated this approach in the regression of log K vs T relationships shown in Fig. 3.

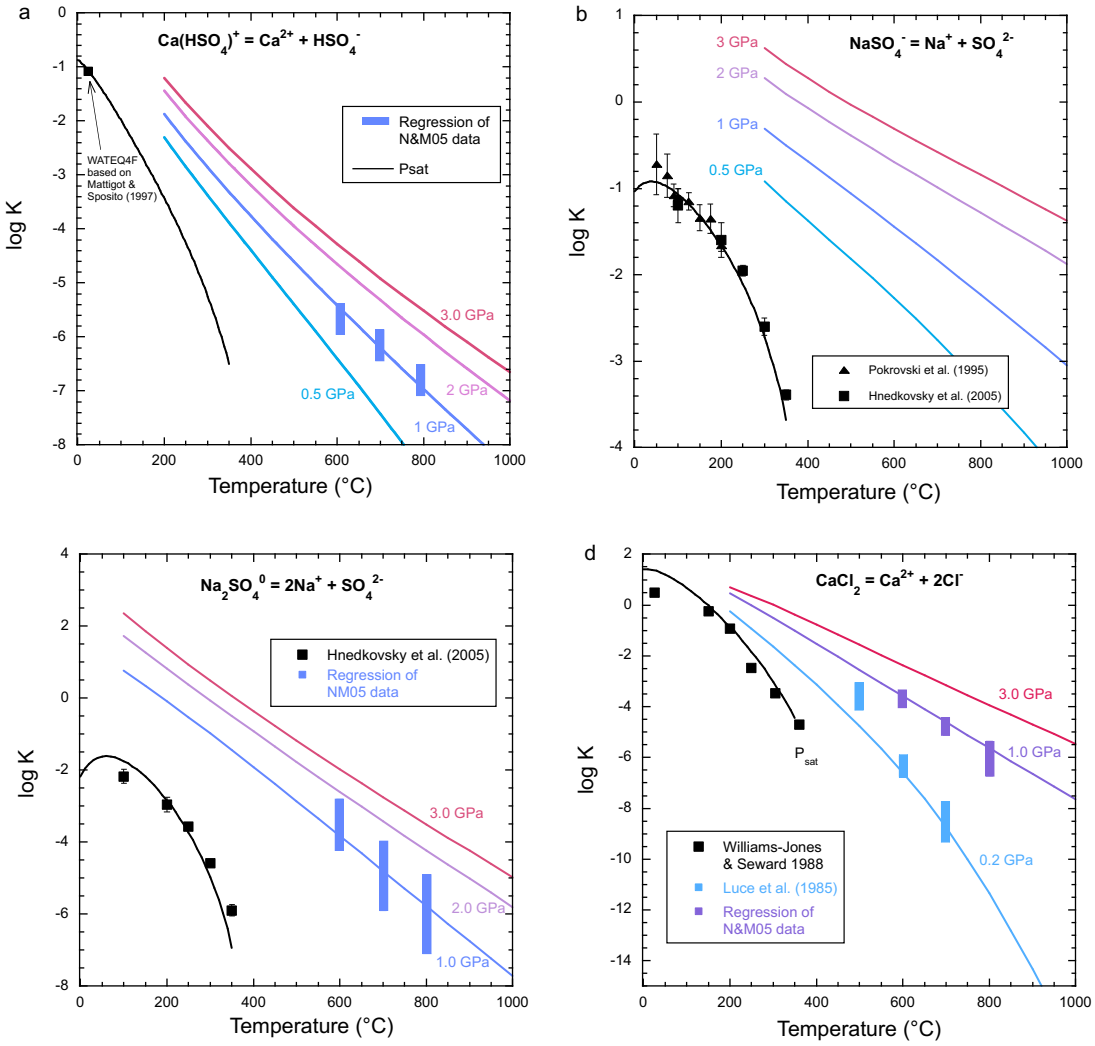

Figure 3 (a-d): Regression of the temperature dependence of equilibrium constants for the aqueous ions and complexes added to the Deep Earth Water (DEW) model in this work. The adopted standard partial molal properties and equation of state coefficients are provided in Table 1.

We tested our equations of state for the Ca- and Na-complexes by predicting equilibrium constants as a function of pressure which in turn were used to preduct anhydrite solubility vs pressure (Fig. S2). Despite a small difference in the slope of the predicted curve with pressure, the overall

agreement with the measured pressure dependence is satisfactory. It suggests that the overall uncertainties of the model are well within about ±0.1 to 0.2 log units, consistent with previous theoretical analyses at elevated temperatures and pressures (Huang & Sverjensky, 2019; Shock & Helgeson, 1988; Sverjensky et al., 2014).

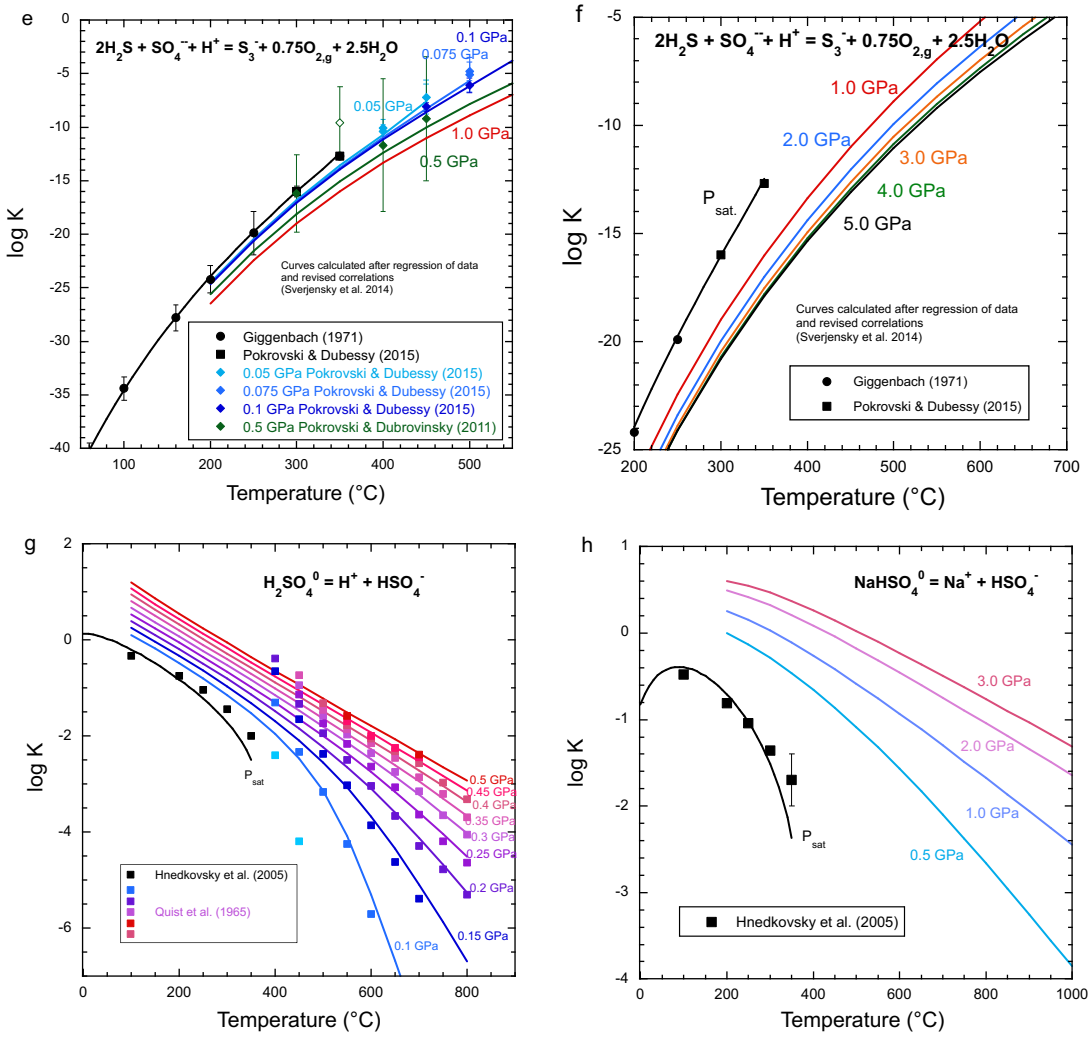

Figure 3 (e-h): Additional S species that were considered but did not play a significant role in the solubility of S in subduction fluids. **(e)** and **(f)** show our regression for the S_3^- ion, showing a weakly negative pressure dependence (negligible beyond ~30 kbar). We used experimental log K data reported by Pokrovski & Dubessy (2015); **(g)** The regression for $H_2SO_4^0$ displays a good fit to the experimental data of Quist et al. (1965) at high temperatures relevant for our calculations; this complex was found to be in negligible concentrations at all conditions investigated (**Tables S1 and S2**). **(h)** $NaHSO_4^0$ was excluded from the regression of Newton and Manning's experimental data due to its poorer fit compared to that of $Na_2SO_4^0$ (Fig. 2a), but was included in the modelling of subduction zone fluids.

Table 2. Standard partial molal properties at 25°C and 1.0 bar and equation of state coefficients for aqueous species contributing to sulfur solubility, used, added or updated in the Deep Earth Water (DEW) model in this study. The parameters are based on experimental solubilities, regression calculations and correlations (see text and Fig. 3).

SPECIES	ΔG_f^{0} [a]	ΔH_f^{0} [a]	S^{0} [b]	C_P^{0} [b]	V^{0} [c]	$a_1\ x10$ [d]	$a_2\ x10^{-2}$ [a,i]	a_3 [e,i]	$a_4\ x10^{-4}$ [f,i]	c_1 [b,i]	$c_2\ x10^{-4}$ [f,i]	$\omega\ x10^{-5}$ [a]
H_2S_{aq} [g]	-6,673	-9,001	30.0	42.8	34.9	6.51	6.77	5.96	-3.06	32.3	4.73	-0.1
HS^- [g]	2,860	-3,850	16.3	-22.6	20.6	5.01	4.98	3.48	-2.98	3.42	-6.27	1.44
HSO_4^- [g]	-180,630	-212,500	30.0	5.3	35.2	8.92[h]	4.21	1.31	-2.95	20.10	-1.96	1.17
SO_4^{2-} [g]	-177,930	-217,400	4.5	-63.9	13.9	8.30	-1.98	-6.21	-2.70	1.64	-18.00	3.15
$CaSO_{4_{aq}}^{0}$	-312,930[g]	-345,900[g]	5.0[g]	-25.0[g]	33.0[h]	8.07[h]	3.40	1.98	-2.92	-5.72	-8.13	0.30
$CaHSO_4^+$	-314,200[j]	-338,235[j]	35.0[k]	70.0[k]	37.0[k]	8.72[k]	4.02	1.47	-2.95	47.39	11.22	0.02[k]
$NaSO_4^-$	-241,780[l]	-275,480[l]	20.4[l]	5.0[l]	41.0[h]	10.12[h]	5.35	0.35	-3.00	21.25	-2.02	1.32
$Na_2SO_{4_{aq}}^{0}$	-305,500[m]	-279,585[m]	27.0[k]	95.0[k]	54.0[h]	12.15[h]	7.28	-1.27	-3.08	64.61	16.32	0.30[k]
$CaCl_{2_{aq}}^{0}$	-193,000[n]	-211,060[n]	19.0[o]	18.0[o]	30.0[h]	7.92[h]	3.26	2.10	-2.91	27.77	0.63	1.20[o]
S_3^-	13,160[p]	10,840[p]	23.0[q]	95.0[q]	77.0[q]	17.24[q]	12.13	-5.34	-3.28	76.58	16.32	1.60[q]
$H_2SO_{4_{aq}}^{0}$	-123,800[r]	-159,845[r]	16.0[r]	20.0[r]	38.0[r]	8.95[h]	4.24	1.29	-2.95	18.81	1.04	0.10
$NaHSO_{4_{aq}}^{0}$	-244,000[m]	-271,575[m]	37.0	73.5	47.7[h]	10.77[h]	5.97	-0.17	-3.03	48.89	11.94	-0.04

[a] cal.mole^{-1}. [b] cal.mole^{-1}.K^{-1}. [c] cm^{-3}.mole^{-1}. [d] cal.mole^{-1}.bar^{-1}. [e] cal.K.mole^{-1}.bar^{-1}. [f] cal.K.mole^{-1}.

[g] Parameters taken from DEW2019 (Huang & Sverjensky, 2019)

[h] Estimated from $\sum v_i a_i = 0$.

[i] Calculated following Sverjensky et al. (2014).

[j] Calculated from logK = -1.08 at 25°C and 1 bar, which assumes the dissociation constant of divalent metal bisulfate complexes is approximately equivalent (Ball & Nordstrom, 1991; Mattigod & Sposito, 1977).

[k] Regression of anhydrite solubility data in Figs. 1a and 3a ($CaHSO_4^+$), 2a and 3c ($Na_2SO_4^0$).

[l] Pokrovski et al. (1995).

[m] Estimated from logK's at the vapor saturation pressure from Hnedkovsky et al. (2005).

[n] Sverjensky et al. (1997).

[o] Regression of AgCl solubility data from (Williams-Jones & Seward, 1989), Ca-silicate solubility data (Luce et al., 1985) and anhydrite solubility data shown in Fig. 3d.

[p] (Pokrovski & Dubessy, 2015)

[q] Regression of Raman speciation (Giggenbach, 1971; Pokrovski & Dubessy, 2015; Pokrovski & Dubrovinsky, 2011) shown in Fig. 3e,f.

[p] Regression of logK's from electrical conductance data from Quist et al. (1965), 0-5 kbar and 100-800°C.

We also investigated the use of our solubility model for calculating anhydrite solubilities in NaCl solutions at low temperatures and pressures. However, our predicted solubilities did not agree with the experimental measurements of Blount & Dickson (1969). The latter measured solubilities of anhydrite in H_2O–NaCl solutions at vapor-saturated conditions, and 0.05 and 0.1 GPa and 100–450°C. The experimental data show a negative temperature dependence at low pressures and temperatures, in marked contrast to the experiments of Newton and Manning (2005) which show a positive temperature dependence at 1 GPa and 600–800°C (see Figs. 1-2). Although our calculations of anhydrite solubility in pure water at vapor-saturated conditions were consistent with the experiments of Blount and Dickson (1969), our model overpredicted the solubilities at low pressures with increasing NaCl concentrations up to 6.0 m owing to high model concentrations of the complex $Na_2SO_4^0$. We note that $Na_2SO_4^0$ is thermodynamically constrained in our model along the liquid-vapor saturation curve by the results of Hnedkovsky et al. (2005)—see Fig. 3c. Consequently, there is a fundamental inconsistency between the results of Blount and Dickson (1969) and Hnedkovsky et al. (2005). The reason for this inconsistency is not clear. We note however that in the Hnedkovsky et al. (2005) conductance study, equilibrium constants of five complexes were obtained by regression, which may have led to over-fitting of the conductance data. It is evident that additional experimental speciation and solubility data are needed. We emphasize that our characterization of sulfate complexes was optimized to match the high-pressure experiments of Newton and Manning (2005) since we are interested in the solubility and speciation of sulfur in subduction zone fluids at pressures of 2 and 3 GPa.

As a further test of the robustness of our models we investigated the possible importance of several additional aqueous sulfur-bearing species were also investigated while fitting the experimental data in Fig. 2a. These included $H_2SO_4^0$, $NaHSO_4^0$, and the trisulfur radical ion S_3^-. First, we note that the experimental study by (Hnedkovsky et al., 2005) provided dissociation constants at vapor-saturated conditions for the $H_2SO_4^0$ and $NaHSO_4^0$ complexes according to the equilibria

$$H_2SO_4^0 \rightleftharpoons H^+ + HSO_4^- \quad \text{(Eq. 6)}$$

$$HSO_4^- \rightleftharpoons H^+ + SO_4^{2-} \quad \text{(Eq. 7)}$$

$$NaHSO_4 \rightleftharpoons Na^+ + HSO_4^- \quad \text{(Eq. 8)}$$

We also retrieved the thermodynamic properties and equation of state parameters of $H_2SO_4^0$ from the experimental data of, who reported equilibrium constants In addition, experimental equilibrium constants for Eqs. 6 and 7 were reported by Quist et al. (1965) based on the electrical conductances of dilute aqueous sulfuric acid solutions at temperatures of 100–800°C and 0–5 kbar (Table 2 and Fig. 3g). It is perhaps significant that our equation of state fit to the extensive dataset obtained by Quist et al. (1969) does not agree at low temperatures and pressures with all the data from Hnedkovsky et al. (2005). At high pressures relevant to the experiments of Newton & Manning (2005), we found that this species was mostly dissociated and did not have any effect on the modeled anhydrite solubilities.

For $NaHSO_4^0$, we used the predictive model of Sverjensky et al. (1997) to estimate the dissociation constant of (Eq. 8) at higher pressures and temperatures (Fig. 3h), but found that this complex did not reproduce the steep increase in anhydrite solubility vs NaCl shown in Fig. 2a. Although a complete thermodynamic model should include every possible species, $Na_2SO_4^0$ and $CaCl_2^0$ appeared to be the most important in this system. Preliminary models indicated that the $NaHSO_4^0$ complex was typically accounting for less than about 10% of the dissolved sulfur species.

Therefore we did not include this complex in the final regression analysis of the solubility data. Nevertheless, we do include preliminary predictions of its thermodynamic properties and equation of state parameters in Table 2. During application of our model to subduction zone mineral assemblages, the $NaHSO_4^0$ did appear to be important under some conditions (see below).

HKF equation of state parameters for the $NaSO_4^-$ complex were provided by (Pokrovski et al., 1995) based on regression of experimental data at the vapor saturation pressure. We refined these parameters using the data from Hnedkovsky et al. (2005) to remain internally consistent with our new species $Na_2SO_4^0$ and $NaHSO_4^0$ (Fig. 3b and Table 2).

We also included the trisulfur radical ion S_3^- in the DEW database, since its importance in geological fluids has been demonstrated (Pokrovski & Dubessy, 2015; Pokrovski & Dubrovinsky, 2011). To constrain the thermodynamic properties of this ion, we regressed available experimental data from Giggenbach (1971), Pokrovski & Dubrovinsky (2011) and Pokrovski & Dubessy (2015), which cover the vapor-saturated pressure-temperature range, as well as 0.1 GPa and 0.5 GPa pressures between 300 and 500°C (Fig. 3e,d). We provide our estimated equation of state coefficients in Table 2. We note that our thermodynamic parameters differ from those reported by Pokrovski and Dubessy (2015), resulting in a negative pressure dependence of log K instead of a positive one. Use of the originally published parameters resulted in an unphysical pressure dependence (Fig. S3); thus we regressed these data as shown in Fig. 3e,d, noting that better experimental constraints are needed at pressures > 0.1 GPa.

2.2. Predictive modelling of subduction zone fluids

We predicted the geochemistry of fluids in equilibrium with mafic and ultramafic mineral assemblages at subduction zone conditions as a function of fO_2. Most of the fluid release in subduction zones is thought to occur via the dehydration of antigorite between 2 and 3 GPa (Schmidt & Poli, 1998; Ulmer & Trommsdorff, 1995). Hence we performed calculations at these two pressures and at 400 to 800°C to encompass both cold and hot subduction zones (**Fig. 4**). We varied fO_2 over 6 orders of magnitude from FMQ-2 to FMQ+4. This wide range in log fO_2 is intended to enable comparison with the similarly wide range reported in the literature (Ague et al., 2022; Debret & Sverjensky, 2017; Iacovino et al., 2020; Padrón-Navarta et al., 2023; Piccoli et al., 2019; Tumiati et al., 2015). We predicted the aqueous speciation and solubilities of major chemical elements Na, K, Mg, Ca, Fe, Al, Si, Cl, C, and S and the pH in equilibrium with model mafic and ultramafic mineral assemblages as a function of fO_2 (Tables S1 and S2). We assumed saturation with a S-bearing mineral to determine the maximum possible concentrations of S in the fluids. Pyrrhotite was stable at reduced conditions, while anhydrite was stable at oxidized conditions (~ΔFMQ>3). Pyrite was stable at intermediate fO_2 around ~FMQ to FMQ+2 (Fig. 6). All calculations assumed a dissolved Cl^- content of 0.5 m, broadly consistent with fluid inclusion data (Scambelluri et al., 2004).

2.2.1. Mafic assemblages

To represent the oceanic crust, we used an eclogitic assemblage consisting of garnet + clinopyroxene + quartz/coesite ± magnetite. At the lowest T (400°C) model runs, lawsonite, talc, chlorite, biotite and quartz were found to represent the equilibrium assemblage. We used simplified garnet and clinopyroxene solid solution compositions based on natural samples of mafic eclogites (Viete et al., 2018). For example, the garnet end-members pyrope ($Mg_3Al_2Si_3O_{12}$), almandine ($Fe_3Al_2Si_3O_{12}$) and grossular ($Ca_3Al_2Si_3O_{12}$) were used in 12:63:25 proportions to buffer fluid

concentrations of Mg, Fe and Ca, respectively. Clinopyroxene was simplified as a 35:20:45 mixture of diopside ($CaMgSi_2O_6$), hedenbergite ($CaFeSi_2O_6$) and jadeite ($NaAlSi_2O_6$). The Cl concentration was fixed at 0.5 m, broadly consistent with measurements of serpentinite-hosted fluid inclusions associated with antigorite breakdown (Scambelluri et al., 2004). Na^+ was calculated in the model by charge balance, but also linearly varied with the concentration of Na_2SO_4, thus being most abundant at high fO_2 and high T (see **Table S1**). We imposed an arbitrary K concentration of 0.1 m; this value is approximately consistent with the observation that Na/K ratios of the fluid inclusions reported by Scambelluri et al. (2004) are relatively constant around 12. Most model runs had final Na concentrations between 0.3 and 0.6 m, giving lower Na/K ratios of 3 to 6, which might be expected for the mafic oceanic crust compared to serpentinite-hosted fluid inclusions. However, we note that high fO_2, high-T model runs had Na concentrations >1 m and up to 6 m at 800°C. The effect of K on S speciation was unimportant in all model runs, representing <0.1 % of the total S budget in all cases (**Tables S1 and S2**). Finally, we fixed the C concentration at 0.1 m, noting that it may be highly variable across different subduction zones (Plank & Manning, 2019).

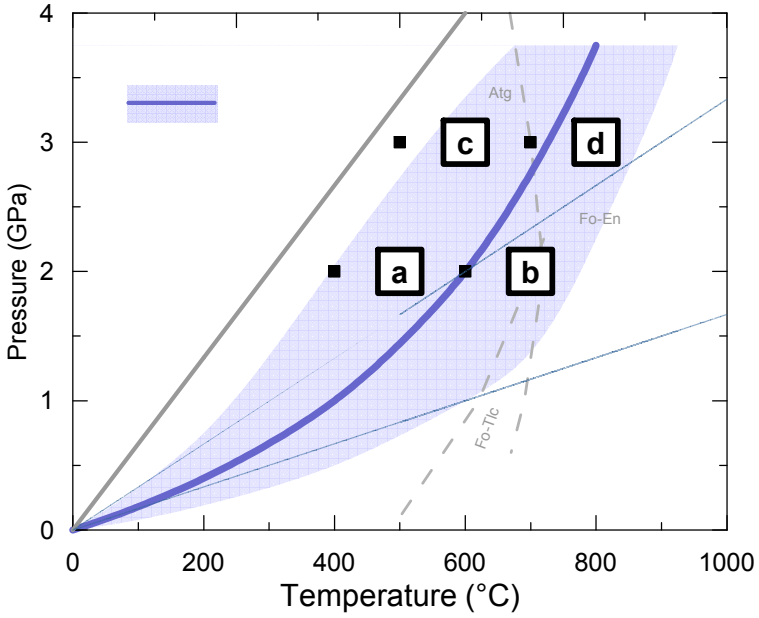

Figure 4: Pressure-temperature diagram showing the range of subduction zone conditions recorded in natural subduction zone metamorphic rocks (purple region; Penniston-Dorland et al., 2015) with the "average" global subduction zone thermal profile (thick purple curve). The "Cold subduction" and "Hot subduction" scenarios depicted in Fig. 5 ([a, c] and [b, d], respectively) are shown here for reference. Additional models were calculated for four more combinations of P-T conditions (black squares), for a total of eight, which are shown in Figs. S4 and S5. Antigorite breakdown reaction from (Ulmer & Trommsdorff, 1995) shown for reference (gray dashed lines) as well as 5°C/km (gray line; "Forbidden Zone"), 10°C/km and 20°C/km geotherms (pale blue lines). Atg: antigorite; Fo: forsterite; En: enstatite; Tlc: talc.

2.2.2. Ultramafic assemblages

The serpentinised mantle lithosphere was represented by ultramafic assemblages consisting of clinopyroxene + tremolite + magnetite ± olivine ± orthopyroxene ± antigorite ± chlorite ± garnet

± hematite + pyrite, pyrrhotite or anhydrite, corresponding to serpentinites at lower T-P and to garnet peridotite at higher T-P. The transition from antigorite to forsterite + enstatite occurs around 600-700 °C (Fig. 4), hence we changed the mineralogy accordingly to satisfy equilibrium in all model runs. No mineral phase could successfully buffer Ca concentration in our model runs due to phase rule violations. Therefore we fixed the Ca concentration at 0.05 m, to approach the average Ca/Na of 0.2 measured in serpentinite-hosted fluid inclusions by Scambelluri et al. (2004). The Cl concentration was fixed at 0.5 m, and Na was used to achieve charge balance. However, this resulted in prohibitively high Na concentrations (>100m) in high fO_2 runs due to the dominance of Na_2SO_4 and $NaSO_4^-$. We overcame this problem by instead using Ca^{2+} to satisfy charge balance, and fixing Na concentration at 0.5 m. This led to somewhat lower total S concentrations in ultramafic fluids at high temperatures compared to mafic fluids, as seen in Fig. 3 of the main text. We refer the reader to Table S2 for a summary of model runs with ultramafic assemblages.

We note that the compositions of olivine, pyroxenes and chlorite in the ultramafic runs are dependent on the imposed fO_2, with Mg# increasing with increasing fO_2, and in all cases equilibrium olivine Mg# is lower than typical mantle values of ~0.9. Hypothetical olivines determined by EQ3 had Mg#'s from ~0.4 at QFM-2 to ~0.85 at QFM+3 (Table S2). This is partly due the fact that magnetite is the only Fe^{3+}-bearing phase in the model (other than hematite in runs where $\log fO_2 > 3$). In natural rocks, some Fe^{3+} is incorporated into pyroxenes, and mantle spinel is not pure magnetite, hence our thermodynamic approach has inherent limitations in dealing with Fe speciation, due to a lack of thermodynamic data. Chlorite Mg#'s similarly varied from 0.7 at QFM-2 to 0.95 at QFM+3. As a comparison, chlorite in natural chlorite harzburgites from the Cerro del Almirez complex have Mg# around 0.95 (Padrón-Navarta et al., 2011). We anticipate that these departures from natural compositions do not significantly change our results because the total concentrations of Fe and Mg in the fluids do not dramatically change with varying fO_2, and importantly since they are lower by factors of 5-10 compared to those of Ca and Na at oxidizing conditions (Tables S1 and S2).

3. Results

The predicted total dissolved sulfur and sulfur speciation in 0.5 m chloride fluids in equilibrium with the mafic eclogite assemblages and pyrrhotite, pyrite, or anhydrite are summarized in Fig. 5. Results are shown for cold and hot subduction paths (see also Figs. S4, S5). A major difference between the two paths is that at higher temperatures the stability field for pyrite contracts significantly (Figs. 5, S4 and S5). The calculated total sulfur solubilities are ~2-10 times higher than previous predictions (e.g. Walters et al., 2020).

It can be seen in Fig. 5 that the bulk of the dissolved sulfur at oxidizing conditions is dominated by $CaHSO_4^+$, and/or $Na–SO_4$ species, with the latter becoming dominant in the hot subduction scenario. At reducing conditions, H_2S and HS^- are dominant. The transition from reduced to oxidized sulfur species occurs over a range of about one $\log fO_2$ unit (**Fig. S6**). At 3 GPa the transition occurs about one $\log fO_2$ unit lower than at 2 GPa. At the pressure-temperature conditions investigated, the total sulfur solubility is highest at oxidized conditions, i.e. when sulfate species are dominant. This behavior is particularly enhanced by the species $CaHSO_4^+$ and $Na_2SO_4^0$, but concentrations of HSO_4^- and SO_4^{2-} also surpass those of reduced species (Fig. 5).

A notable feature of Fig. 5 is that pyrite is stable at ~FMQ+1 to +2, in the region where sulfate species become dominant. As a consequence, the total dissolved sulfur concentrations in equilibrium with pyrite reach values as high as about 3.0 m. This highlights the importance of the

new complexes $CaHSO_4^+$ and $Na_2SO_4^0$ on pyrite solubility. As fO_2 is increased further, anhydrite becomes stable, and the total S solubility becomes constant. At the highest pressure and temperature (3 GPa and 800°C), there is also a narrow log fO_2 range where no S-bearing phase was found to saturate (Fig. 5d), suggesting maximum efficiency in S recycling at these conditions.

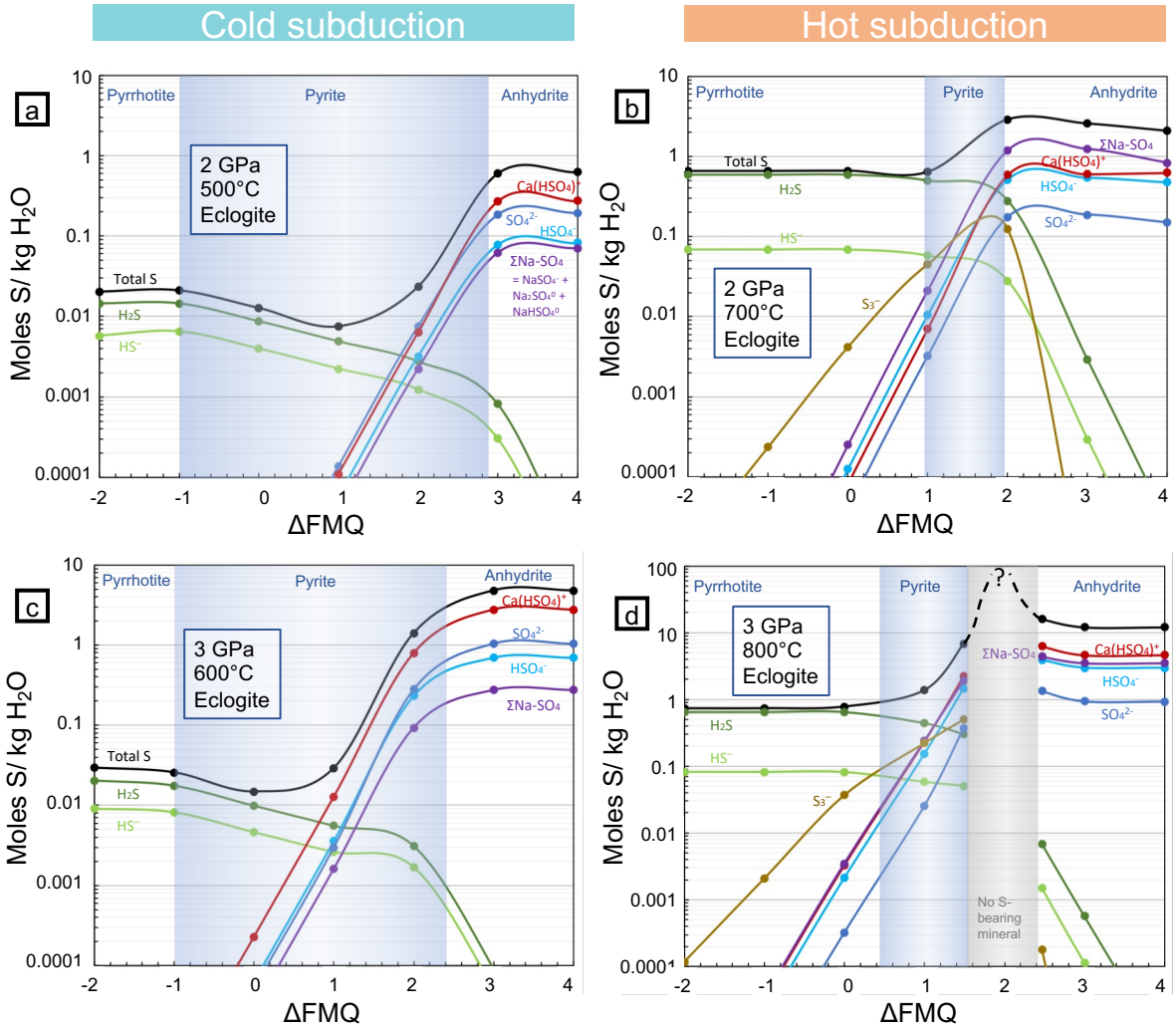

Figure 5: Predicted sulfur solubility and speciation in aqueous fluids as a function of log fO_2 (relative to FMQ) in equilibrium with a mafic eclogitic mineral assemblage plus a S-bearing mineral. Panels (a) and (c) represent cold subduction, whereas (b) and (d) represent hot subduction (see text). Note the wider pyrite stability field (blue shaded region) for cold subduction, and the steep increase in sulfate species, with high anhydrite solubility at all conditions investigated. In (d), there is a small ΔFMQ range in which no S-bearing phase could saturate.

In Fig. 6, we show the calculated total sulfur concentration of slab fluids in equilibrium with mafic and ultramafic lithologies at different P-T-fO_2 conditions. Although rock type causes subtle differences in the calculated sulfur contents, the overall behavior is similar. Fig. 6 illustrates the important effect of temperature on sulfur solubility, which increases by about one order of magnitude per 100°C. However, at lower temperatures there is a steeper increase in sulfur solubility with increasing fO_2. For example, at 500°C and 3 GPa, total dissolved sulfur increases by >3 orders of magnitude with increasing fO_2.

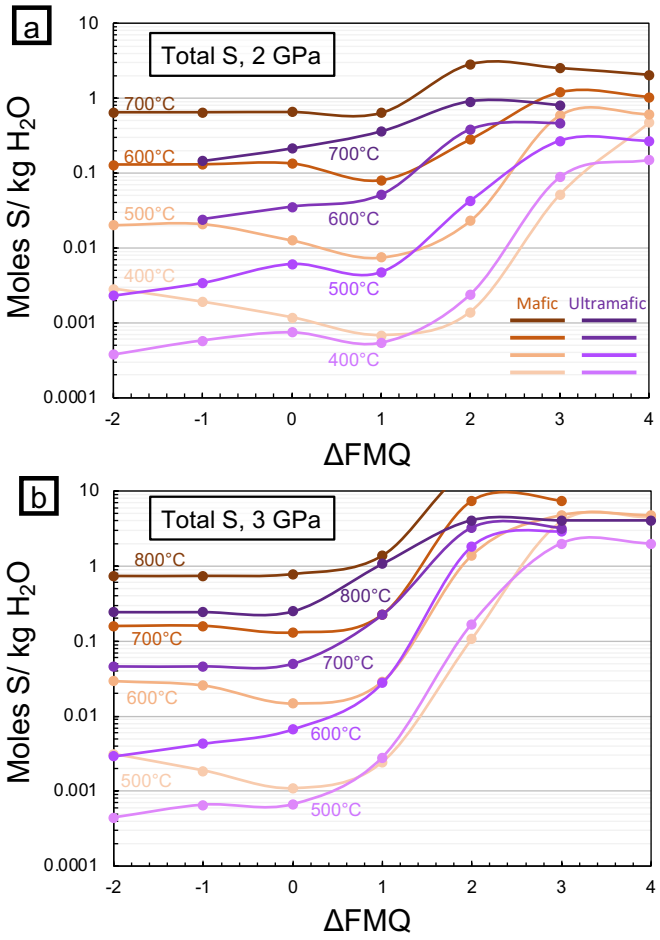

Figure 6: Comparison of predicted total dissolved sulfur in fluids in equilibrium with mafic eclogite and ultramafic (serpentinite/garnet peridotite) assemblages. Isotherms are shifted to 100°C higher at 3 GPa, equivalent to a ~5°C/km geothermal gradient, consistent with the average subduction gradients derived from natural rocks (see Fig. S-5). The similar sulfur solubilities of the two mineral assemblages shows that P-T-fO_2 exert the primary control on sulfur solubility. Detailed S speciation shown in Figs. S-6 (mafic) and S-7 (ultramafic).

4. Discussion

Our results suggest that at FMQ+1.0 to +3.0, significant concentrations of oxidized sulfur species should be preferentially released into slab fluids as a function of temperature and pressure. These fO_2 conditions are comparable to findings by several authors suggesting that slab dehydration releases oxidizing fluids (Debret & Sverjensky, 2017; Iacovino et al., 2020; Walters et al., 2020). We therefore use our sulfur speciation model to evaluate the extent of sulfur isotopic fractionation between fluid and subducting slab.

4.1. Implications for sulfur isotopic fractionation

A central question surrounding the recycling of sulfur in subduction zones concerns the relative contributions from sediments and subducted oceanic lithosphere. We focus on the altered oceanic crust and serpentinised mantle lithosphere in this work because they represent a much larger

volume and are likely a dominant source of subducted sulfur (e.g. de Moor et al., 2022). Although subducted sedimentary sulfur has a large range of isotopic compositions from very negative $\delta^{34}S$ pyrite to high positive $\delta^{34}S$ in seawater-derived sulfate (Alt et al., 1993), the sedimentary flux and its sulfur content vary widely across different subduction zones. Hence, we wish to constrain the isotopic signature of sulfur in slab fluids before any interaction with overlying sedimentary layers (cf. Ague et al., 2022; Padrón-Navarta et al., 2023), by considering fluids in equilibrium with the subducted mafic crust and mantle lithosphere.

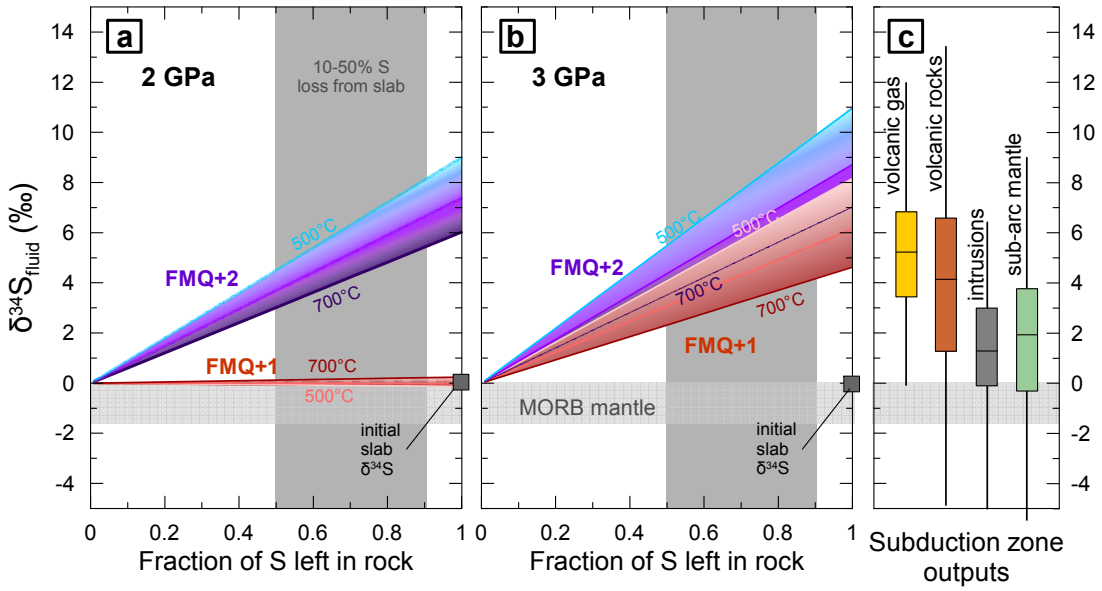

Figure 7: Predicted sulfur isotope compositions of slab fluids relative to a subducting slab with initial $\delta^{34}S$ of 0‰ at (a) 2.0 GPa and (b) 3.0 GPa. The calculations use predicted proportions of sulfate and sulfide species to estimate isotopic fractionation between fluid and rock (see text). Calculations are shown for FMQ+1 and FMQ+2, often attributed to subduction fluids. Dark grey field shows the estimated recycling efficiency of sulfur of 10-50% (see text), and pale grey horizontal band corresponds to the estimates of the MORB mantle (see refs in Rezeau et al., 2023). The importance of sulfate-bearing species at lower fO_2 at 3 GPa compared to 2 GPa translates to higher $\delta^{34}S$ values. Our calculations match the range of measured $\delta^{34}S$ values in subduction zone outputs shown in (c) (Rezeau et al., 2023).

We address this question by calculating the equilibrium isotopic fractionation between released fluids and subducting slab, which relies on the proportion of oxidized sulfur in the fluid, the nature of the solid S-bearing phase, and temperature. We used the T-dependent fractionation factors $\alpha_{SO_4^{2-}-H_2S}$ from Ohmoto and Lasaga (1982), and α_{po-H_2S} and α_{py-H_2S} from Ohmoto (1979), assuming negligible isotopic fractionation between sulfur species having the same oxidation state. Pressure and fO_2 are not explicit variables in the calculations, but they control the sulfur speciation of the fluid and mineral stabilities (Figs. 5, 6 and S6a). Consequently, they ultimately play a crucial role in the degree of sulfur isotopic fractionation between fluid and rock (Fig. S6b). At 2 GPa, oxidized sulfur species become dominant above FMQ+1.5, whereas at 3 GPa they become dominant at FMQ+0.5 (Fig. S6a). At these conditions, pyrite is the dominant S-bearing mineral. Since the oxidized species are generally more ^{34}S-rich than their reduced counterparts (Ohmoto, 1979), slab fluids in equilibrium with pyrite at moderate fO_2 will be

isotopically enriched (Figs. 7, S6b), while pyrite will become progressively depleted as sulfur is released to the fluids.

The resulting $\delta^{34}S$ signature of slab fluids is illustrated in Fig. 7, assuming closed-system equilibrium isotope fractionation, and an initial slab $\delta^{34}S$ signature of 0 ‰, generally consistent with subducted altered oceanic crust (e.g. Rezeau et al., 2023). It can be seen in Fig. 7 that, for a recycling efficiency of 10-50% (Li et al., 2020; Taracsák et al., 2023; Wallace, 2005; Walters et al., 2020), the magnitude of sulfur isotope fractionation expected between fluid and slab largely reproduces the global range of subduction outputs compiled by Rezeau et al. (2023). Therefore, without any external input of sulfur (e.g. sedimentary sulfides, seawater sulfate), the coexistence of sulfate-rich fluids with pyrite at the P-T-fO_2 conditions expected in subduction zones produces important isotope fractionation. We therefore consider it likely that the flux of oxidized sulfur from these fluids can oxidize the mantle wedge and elevate its overall $\delta^{34}S$ signature, as previously suggested (de Moor et al., 2022; Muth & Wallace, 2021; Taracsák et al., 2023; Walters et al., 2020). Nevertheless, we acknowledge that some subducting slabs may release fluids with lower fO_2, which would be instead dominated by reduced sulfur species with minimal isotopic fractionation (e.g. Li et al., 2020). We also recognize that isotopic fractionation in natural systems would be more complex, as the condition of isotopic equilibrium may not always be achieved and Rayleigh fractionation can occur during reprecipitation of metasomatic sulfides (Walters et al., 2019). Nonetheless, the widespread coexistence between high concentrations of aqueous sulfate species and pyrite, as suggested by our speciation model, should to a first order produce isotopically enriched slab fluids of the scale presented here.

We also note that while more oxidized fluids are expected to be more sulfur-rich, the higher pyrite solubility at higher temperatures suggests that this is where sulfur recycling is most efficient. However, higher temperatures are also associated with less isotopic fractionation (Fig. 7). Therefore, fluids with higher oxidizing power, e.g. rich in sulfate species, may not necessarily be the most ^{34}S-rich. Ultimately, the sulfur isotopic signatures of the mantle wedge and of subduction outputs depend on several factors, including the subduction P-T path, the relative proportions of mantle- and fluid-derived sulfur, and the initial $\delta^{34}S$ in the slab. Our results provide a basis to quantitatively assess the sulfur isotopic variability of fluid components from subducting slabs, upon which subsequent fluid-melt-rock interactions, additional sulfur sources, and magmatic processes can be superimposed. The large range of $\delta^{34}S$ values observed in subduction zone outputs in part reflects the expected variability in sulfur contents and isotopic signatures of slab fluids (Figs. 5-7).

5. Conclusions

We have integrated high pressure experimental anhydrite solubility data in pure water and NaCl solutions (Newton and Manning, 2005) into an aqueous speciation and solubility model using the complexes $CaHSO_4^+$, $CaCl_2^0$ and $Na_2SO_4^0$. As a result we have provided a framework for interpreting sulfur isotopic fractionation between fluids and subducting slabs as a function of fO_2. At moderately oxidizing conditions of FMQ+1 to FMQ+2, predicted high pressure sulfur-bearing fluids in equilibrium with subducting mafic and ultramafic mineral assemblages and pyrite have much higher solubilities of oxidized sulfur species than previously recognised. This produces isotopic fractionation between fluids and subducting slabs, thus our results are consistent with the hypothesis that slab fluids could oxidize the mantle wedge with ^{34}S-rich sulfate species.

Acknowledgements

This material is based upon work supported by the U.S. Department of Energy, Office of Science, Basic Energy Sciences, Geosciences program under Award Number DE-SC0019830 as well as NSF Petrology and Geochemistry Grant Number 2032039.

Open Research

All calculations in this work were performed with the software EQ3 (Wolery, 1992), with chemical species defined in the Extended Deep Earth Water model (Huang & Sverjensky, 2019) and this work (Table 2).

References

Ague, J. J., Tassara, S., Holycross, M. E., Li, J. L., Cottrell, E., Schwarzenbach, E. M., et al. (2022). Slab-derived devolatilization fluids oxidized by subducted metasedimentary rocks. *Nature Geoscience*. https://doi.org/10.1038/s41561-022-00904-7

Alt, J. C., Shanks, W. C., & Jackson, M. C. (1993). Cycling of sulfur in subduction zones: The geochemistry of sulfur in the Mariana Island Arc and back-arc trough. *Earth and Planetary Science Letters*, *119*(4), 477–494. https://doi.org/10.1016/0012-821X(93)90057-G

Ball, J. W., & Nordstrom, D. K. (1991). User's manual for wateq4f, with revised thermodynamic data base and test cases for calculating speciation of major, trace, and redox elements in natural waters. *US Geological Survey*.

Bebout, G. E., & Penniston-Dorland, S. C. (2016, January 1). Fluid and mass transfer at subduction interfaces-The field metamorphic record. *Lithos*. Elsevier. https://doi.org/10.1016/j.lithos.2015.10.007

Bénard, A., Klimm, K., Woodland, A. B., Arculus, R. J., Wilke, M., Botcharnikov, R. E., et al. (2018). Oxidising agents in sub-arc mantle melts link slab devolatilisation and arc magmas. *Nature Communications*, *9*(1), 1–10. https://doi.org/10.1038/s41467-018-05804-2

Blount, C. W., & Dickson, F. W. (1969). The solubility of anhydrite (CaSO4) in NaCl-H2O from 100 to 450°C and 1 to 1000 bars. *Geochimica et Cosmochimica Acta*, *33*(2), 227–245. https://doi.org/10.1016/0016-7037(69)90140-9

Brounce, M., Reagan, M. K., Kelley, K. A., Cottrell, E., Shimizu, K., & Almeev, R. (2021). Covariation of Slab Tracers, Volatiles, and Oxidation During Subduction Initiation. *Geochemistry, Geophysics, Geosystems*, *22*(6), 1–30. https://doi.org/10.1029/2021GC009823

Carmichael, I. S. E. (1991). The redox states of basic and silicic magmas: a reflection of their source regions? *Contributions to Mineralogy and Petrology*, *106*(2), 129–141. https://doi.org/10.1007/BF00306429

Class, C., Miller, D. M., Goldstein, S. L., & Langmuir, C. H. (2000). Distinguishing melt and fluid subduction components in Umnak Volcanics, Aleutian Arc. *Geochemistry, Geophysics, Geosystems*, *1*(6). https://doi.org/10.1029/1999GC000010

Colin, A., Schmidt, C., Pokrovski, G. S., Wilke, M., Borisova, A. Y., & Toplis, M. J. (2020). In situ determination of sulfur speciation and partitioning in aqueous fluid-silicate melt systems. *Geochemical Perspectives Letters*, 31–35. https://doi.org/10.7185/geochemlet.2020

Creaser, E. C., Steele-MacInnis, M., & Tutolo, B. M. (2022). A model for the solubility of anhydrite in H2O-NaCl fluids from 25 to 800 °C, 0.1 to 1400 MPa, and 0 to 60 wt% NaCl: Applications to hydrothermal ore-forming systems. *Chemical Geology*, *587*. https://doi.org/10.1016/j.chemgeo.2021.120609

Debret, B., & Sverjensky, D. A. (2017). Highly oxidising fluids generated during serpentinite breakdown in subduction zones/704/2151/209/704/2151/431/119/118 article. *Scientific Reports*, *7*(1), 1–6. https://doi.org/10.1038/s41598-017-09626-y

Evans, K. A. (2012). The redox budget of subduction zones. *Earth-Science Reviews*, *113*(1–2), 11–32. https://doi.org/10.1016/j.earscirev.2012.03.003

Giggenbach, W. (1971). Blue solutions of sulfur in water at elevated temperatures. *Inorganic Chemistry*, *10*(6), 1306–1308. https://doi.org/10.1021/ic50100a043

Grove, T., Parman, S., Bowring, S., Price, R., & Baker, M. (2002). The role of an H2O-rich fluid component in the generation of primitive basaltic andesites and andesites from the Mt. Shasta region, N California. *Contributions to Mineralogy and Petrology*, *142*(4), 375–396. https://doi.org/10.1007/s004100100299

Hnedkovsky, L., Wood, R. H., & Balashov, V. N. (2005). Electrical conductances of aqueous Na2so4, H 2so4, and their mixtures: Limiting equivalent ion conductances, dissociation constants, and speciation to 673 K and 28 MPa. *Journal of Physical Chemistry B*, *109*(18), 9034–9046. https://doi.org/10.1021/jp045707c

Huang, F., & Sverjensky, D. A. (2019). Extended Deep Earth Water Model for predicting major element mantle metasomatism. *Geochimica et Cosmochimica Acta*, *254*, 192–230. https://doi.org/10.1016/j.gca.2019.03.027

Iacovino, K., Guild, M. R., & Till, C. B. (2020). Aqueous fluids are effective oxidizing agents of the mantle in subduction zones. *Contributions to Mineralogy and Petrology*, *175*(4), 1–21. https://doi.org/10.1007/s00410-020-1673-4

Kessel, R., Schmidt, M. W., Ulmer, P., & Pettke, T. (2005). Trace element signature of subduction-zone fluids, melts and supercritical liquids at 120-180 km depth. *Nature*, *437*(7059), 724–727. https://doi.org/10.1038/nature03971

Li, J. L., Schwarzenbach, E. M., John, T., Ague, J. J., Huang, F., Gao, J., et al. (2020). Uncovering and quantifying the subduction zone sulfur cycle from the slab perspective. *Nature Communications*, *11*(1), 1–12. https://doi.org/10.1038/s41467-019-14110-4

Luce, R. W., Cygan, G. L., Hemley, J. J., & D'angelo, W. M. (1985). Some mineral stability relations in the system CaO□MgO□SiO2□H2O□HCl. *Geochimica et Cosmochimica Acta*, *49*(2), 525–538. https://doi.org/10.1016/0016-7037(85)90044-4

Manning, C. E. (2004). The chemistry of subduction-zone fluids. *Earth and Planetary Science Letters*, *223*(1–2), 1–16. https://doi.org/10.1016/j.epsl.2004.04.030

Mattigod, S. V., & Sposito, G. (1977). Estimated Association Constants for Some Complexes of Trace Metals with Inorganic Ligands. *Soil Science Society of America Journal*, *41*(6), 1092–1097. https://doi.org/10.2136/sssaj1977.03615995004100060015x

de Moor, J. M., Fischer, T. P., & Plank, T. (2022). Constraints on the sulfur subduction cycle in Central America from sulfur isotope compositions of volcanic gases. *Chemical Geology*, *588*, 120627. https://doi.org/https://doi.org/10.1016/j.chemgeo.2021.120627

Muth, M. J., & Wallace, P. J. (2021). Slab-derived sulfate generates oxidized basaltic magmas in the southern Cascade arc (California, USA). *Geology*, *49*(10), 1177–1181. https://doi.org/10.1130/g48759.1

Newton, R. C., & Manning, C. E. (2005). Solubility of anhydrite, CaSO4, in NaCl-H2O solutions at high pressures and temperatures: Applications to fluid-rock interaction. *Journal of Petrology*, *46*(4), 701–716. https://doi.org/10.1093/petrology/egh094

Ohmoto, H. (1979). Isotopes of sulfur and carbon. *Geochemistry of Hydrothermal Ore Deposits*.

Ohmoto, H., & Lasaga, A. C. (1982). Kinetics of reactions between aqueous sulfates and sulfides in hydrothermal systems. *Geochimica et Cosmochimica Acta*, *46*(10), 1727–1745. https://doi.org/10.1016/0016-7037(82)90113-2

Padrón-Navarta, J. A., Sánchez-Vizcaí, V. L., Garrido, C. J., & Gómez-Pugnaire, M. T. (2011). Metamorphic record of high-pressure dehydration of antigorite serpentinite to chlorite harzburgite in a subduction setting (Cerro del Almirez, Nevado-Filábride complex, Southern Spain). *Journal of Petrology*, *52*(10), 2047–2078. https://doi.org/10.1093/petrology/egr039

Padrón-Navarta, J. A., López Sánchez-Vizcaíno, V., Menzel, M. D., Gómez-Pugnaire, M. T., & Garrido, C. J. (2023). Mantle wedge oxidation from deserpentinization modulated by sediment-derived fluids. *Nature Geoscience*, *16*(March). https://doi.org/10.1038/s41561-023-01127-0

Parkinson, I. J., & Arculus, R. J. (1999). The redox state of subduction zones: Insights from arc-peridotites. *Chemical Geology*, *160*(4), 409–423. https://doi.org/10.1016/S0009-2541(99)00110-2

Penniston-Dorland, S. C., Kohn, M. J., & Manning, C. E. (2015). The global range of subduction zone thermal structures from exhumed blueschists and eclogites: Rocks are hotter than models. *Earth and Planetary Science Letters*, *428*, 243–254. https://doi.org/10.1016/j.epsl.2015.07.031

Piccoli, F., Hermann, J., Pettke, T., Connolly, J. A. D., Kempf, E. D., & Vieira Duarte, J. F. (2019). Subducting serpentinites release reduced, not oxidized, aqueous fluids. *Scientific Reports*, *9*(1), 1–7. https://doi.org/10.1038/s41598-019-55944-8

Plank, T., & Manning, C. E. (2019). Subducting carbon. *Nature*, *574*(7778), 343–352. https://doi.org/10.1038/s41586-019-1643-z

Pokrovski, G. S., & Dubessy, J. (2015). Stability and abundance of the trisulfur radical ion S3- in hydrothermal fluids. *Earth and Planetary Science Letters*, *411*, 298–309. https://doi.org/10.1016/j.epsl.2014.11.035

712 Pokrovski, G. S., & Dubrovinsky, L. S. (2011). The S3- ion is stable in geological fluids at elevated temperatures
713 and pressures. *Science*, *331*(6020), 1052–1054. https://doi.org/10.1126/science.1199911
714 Pokrovski, G. S., Schott, J., & Sergeyev, A. S. (1995). Experimental determination of the stability constants of
715 NaSO4− and NaB (OH)40 in hydrothermal solutions using a new high-temperature sodium-selective glass
716 electrode — Implications for boron isotopic fractionation. *Chemical Geology*, *124*(3–4), 253–265.
717 https://doi.org/10.1016/0009-2541(95)00057-S
718 Quist, A. S., Marshall, W. L., & Jolley, H. R. (1965). Electrical conductances of aqueous solutions at high
719 temperature and pressure. II. The conductances and ionization constants of sulfuric acid-water solutions from
720 0 to 800° and at pressures up to 4000 bars. *Journal of Physical Chemistry*, *69*(8), 2726–2735.
721 https://doi.org/10.1021/j100892a040
722 Rezeau, H., Jagoutz, O., Beaudry, P., Izon, G., Kelemen, P., & Ono, S. (2023). The role of immiscible sulfides for
723 sulfur isotope fractionation in arc magmas: Insights from the Talkeetna island arc crustal section, south-central
724 Alaska. *Chemical Geology*, *619*. https://doi.org/10.1016/j.chemgeo.2023.121325
725 Richards, J. P. (2011). HIGH Sr/Y ARC MAGMAS AND PORPHYRY Cu Mo Au DEPOSITS: JUST ADD
726 WATER. *Economic Geology*, *106*(7), 1075–1081. https://doi.org/10.2113/econgeo.106.7.1075
727 Scambelluri, M., Fiebig, J., Malaspina, N., Müntener, O., & Pettke, T. (2004). Serpentinite Subduction: Implications
728 for Fluid Processes and Trace-Element Recycling. *International Geology Review*, *46*(7), 595–613.
729 https://doi.org/10.2747/0020-6814.46.7.595
730 Scambelluri, M., Pettke, T., Rampone, E., Godard, M., & Reusser, E. (2014). Petrology andtrace element budgets of
731 high-pressure peridotites indicate subduction dehydration of serpentinized mantle (cima di Gagnone, Central
732 Alps, Switzerland). *Journal of Petrology*, *55*(3), 459–498. https://doi.org/10.1093/petrology/egt068
733 Schmidt, C., & Seward, T. M. (2017). Raman spectroscopic quantification of sulfur species in aqueous fluids: Ratios
734 of relative molar scattering factors of Raman bands of H2S, HS−, SO2, HSO4−, SO42−, S2O32−, S3− and
735 H2O at ambient conditions and information on changes with pressure and temperature. *Chemical Geology*,
736 *467*, 64–75. https://doi.org/10.1016/j.chemgeo.2017.07.022
737 Schmidt, M. W., & Poli, S. (1998). Experimentally based water budgets for dehydrating slabs and consequences for
738 arc magma generation. *Earth and Planetary Science Letters*, *163*(1–4), 361–379.
739 https://doi.org/10.1016/S0012-821X(98)00142-3
740 Shock, E. L., & Helgeson, H. C. (1988). Calculation of the thermodynamic and transport properties of aqueous
741 species at high pressures and temperatures: Correlation algorithms for ionic species and equation of state
742 predictions to 5 kb and 1000°C. *Geochimica et Cosmochimica Acta*, *52*(8), 2009–2036.
743 https://doi.org/10.1016/0016-7037(88)90181-0
744 Shock, E. L., Helgeson, H. C., & Sverjensky, D. A. (1989). Calculation of the thermodynamic and transport
745 properties of aqueous species at high pressures and temperatures: Standard partial molal properties of
746 inorganic neutral species. *Geochimica et Cosmochimica Acta*, *53*(9), 2157–2183.
747 https://doi.org/10.1016/0016-7037(89)90341-4
748 Sverjensky, D.A., Shock, E. L., & Helgeson, H. C. (1997). Prediction of the thermodynamic properties of aqueous
749 metal complexes to 1000°C and 5 kb. *Geochimica et Cosmochimica Acta*, *61*(7), 1359–1412.
750 https://doi.org/10.1016/S0016-7037(97)00009-4
751 Sverjensky, Dimitri A. (2019). Thermodynamic modelling of fluids from surficial to mantle conditions. *Journal of*
752 *the Geological Society*, *176*(2), 348–374. https://doi.org/10.1144/jgs2018-105
753 Sverjensky, Dimitri A., Harrison, B., & Azzolini, D. (2014). Water in the deep Earth: The dielectric constant and the
754 solubilities of quartz and corundum to 60kb and 1200°C. *Geochimica et Cosmochimica Acta*, *129*, 125–145.
755 https://doi.org/10.1016/j.gca.2013.12.019
756 Taracsák, Z., Mather, T. A., Ding, S., Plank, T., Brounce, M., Pyle, D. M., et al. (2023). Sulfur from the subducted
757 slab dominates the sulfur budget of the mantle wedge under volcanic arcs. *Earth and Planetary Science*
758 *Letters*, *602*, 117948. https://doi.org/10.1016/j.epsl.2022.117948
759 Tomkins, A. G., & Evans, K. A. (2015). Separate zones of sulfate and sulfide release from subducted mafic oceanic
760 crust. *Earth and Planetary Science Letters*, *428*, 73–83. https://doi.org/10.1016/j.epsl.2015.07.028
761 Tumiati, S., Godard, G., Martin, S., Malaspina, N., & Poli, S. (2015). Ultra-oxidized rocks in subduction mélanges?
762 Decoupling between oxygen fugacity and oxygen availability in a Mn-rich metasomatic environment. *Lithos*,
763 *226*, 116–130. https://doi.org/10.1016/j.lithos.2014.12.008
764 Ulmer, P., & Trommsdorff, V. (1995). Serpentine Stability to Mantle Depths and Subduction-Related Magmatism.
765 *Science*, *268*(5212), 858–861. https://doi.org/10.1126/science.268.5212.858

766 Viete, D. R., Hacker, B. R., Allen, M. B., Seward, G. G. E., Tobin, M. J., Kelley, C. S., et al. (2018). Metamorphic
767 records of multiple seismic cycles during subduction. *Science Advances*, *4*(3).
768 https://doi.org/10.1126/sciadv.aaq0234
769 Wallace, Paul J. (2005). Volatiles in subduction zone magmas: Concentrations and fluxes based on melt inclusion
770 and volcanic gas data. *Journal of Volcanology and Geothermal Research*, *140*(1–3), 217–240.
771 https://doi.org/10.1016/j.jvolgeores.2004.07.023
772 Wallace, P.J. (2001). Volcanic SO 2 emissions and the abundance and distribution of exsolved gas in magma bodies.
773 *Journal of Volcanology and Geothermal Research*, *108*(1–4), 85–106. https://doi.org/10.1016/S0377-
774 0273(00)00279-1
775 Walters, J. B., Cruz-Uribe, A. M., & Marschall, H. R. (2019). Isotopic Compositions of Sulfides in Exhumed High-
776 Pressure Terranes: Implications for Sulfur Cycling in Subduction Zones. *Geochemistry, Geophysics,*
777 *Geosystems*, *20*(7), 3347–3374. https://doi.org/10.1029/2019GC008374
778 Walters, J. B., Cruz-Uribe, A. M., & Marschall, H. R. (2020). Sulfur loss from subducted altered oceanic crust and
779 implications for mantle oxidation. *Geochemical Perspectives Letters*, 36–41.
780 https://doi.org/10.7185/geochemlet.2011
781 Wilkinson, J. J. (2013, November). Triggers for the formation of porphyry ore deposits in magmatic arcs. *Nature*
782 *Geoscience*. https://doi.org/10.1038/ngeo1940
783 Williams-Jones, A. E., & Seward, T. M. (1989). The stability of calcium chloride ion pairs in aqueous solutions at
784 temperatures between 100 and 360°C. *Geochimica et Cosmochimica Acta*, *53*(2), 313–318.
785 https://doi.org/10.1016/0016-7037(89)90383-9
786 Wolery, T. J. (1992). *EQ3/6, a software package for geochemical modeling of aqueous systems: package overview*
787 *and installation guide (version 7.0)*. Lawrence Livermore National Lab.
788